STM JOURNALS

Journal of
Polymer & Composites

https://journals.stmjournals.com/jopc

ISSN: 2321-2810 (Online)
ISSN: 2321-8525 (Print)
Volume 14, Issue 4, 2026
DOI (Journal): 10.37591/JoPC

Research JoPC

Chlorophyll-Mimicking $Ti_3C_2T_x$ MXene-Conjugated Polymer Nanocomposites: Nature-Inspired Exciton Funneling Architecture for Ultrahigh Photon-to-Electron Conversion in Organic Solar Cells

Krupal Pawar[1,*], Shekhar Rahane[2], Neha Shirsath[3], Rajeshkumar Sambhe[4], Gokul Mahajan[5], Vasudha Patil[6]

Abstract

Green plant photosynthetic machinery is one of the most efficient natural systems for harvesting solar energy and converting it into useable electronic charge. Specifically, chlorophyll molecules in the Light-Harvesting Complex II (LHC-II) achieve nearly unity quantum yield via a well-organized Förster Resonance Energy Transfer (FRET) mechanism that enables excitons to migrate towards reaction centers. This study presents a bio-inspired nanocomposite architecture using two-dimensional $Ti_3C_2T_x$ MXene nanosheets functionalized with chlorophyll-mimicking porphyrin anchoring layers, incorporated with a ternary blend of conjugated polymers: P3HT, PTB7-Th, and a narrow band gap non-fullerene acceptor polymer. MXene nanosheets enhance light absorption by up to 340% at wavelengths 400–750 nm due to plasmonic properties, create fast charge transport pathways, and allow work function adjustment between 4.2 and 5.1 eV. The porphyrin-functionalized surfaces provide a directionally controlled FRET cascade directing energy from high bandgap donor P3HT (1.9 eV) to intermediate bandgap donor PTB7-Th (1.58 eV) to low bandgap acceptor ITIC-4F (1.26 eV), analogous to energy transfer from antennae to reaction center in Photosystem II. Optimized OSCs exhibit a certified power conversion efficiency (PCE) of 19.7 ± 0.3%, external quantum efficiency >92%, open circuit voltage of 0.96 V, short circuit current density of 26.4 mA/cm², and fill factor of 78.1%, representing >37% improvement over conventional OSCs. Time-resolved photoluminescence, transient absorption spectroscopy, and density functional theory simulations confirm efficient multi-component energy transfer and strong electronic coupling among molecular species.

***Author for Correspondence**
Krupal Pawar
E-mail: krupalpawar@gmail.com

[1]Assistant Professor, Department of Mechanical Engineering, Rajiv Gandhi College of Engineering, Savitribai Phule Pune University (SPPU), Karjule Harya, Dist. Ahilyanagar, Maharashtra, India
[2]Assistant Professor, Department of Basic Sciences, Nutan Maharashtra Institute of Engineering & Technology, Savitribai Phule Pune University (SPPU), Pune, Maharashtra, India
[3]Assistant Professor, Department of Basic Sciences Engineering, Sandip Institute of Technology and Management, Savitribai Phule Pune University (SPPU), Dist. Nashik, Maharashtra, India
[4]Professor, Department of Mechanical Engineering, Jawaharlal Darda Institute of Engineering & Technology, Sant Gadge Baba Amravati University (SGBAU), Yavatmal, Maharashtra, India
[5]Assistant Professor, Department of Mechanical Engineering, Shatabdi Institute of Engineering and Research, Savitribai Phule Pune University (SPPU), Dist. Nashik, Maharashtra, India
[6]Assistant Professor, Department of Artificial Intelligence & Data Science, Shri Chhatrapati Shivaji Maharaj College of Engineering, Savitribai Phule Pune University (SPPU), Nepti, Dist. Ahilyanagar, Maharashtra, India

Received Date: June 12, 2026
Accepted Date: June 24, 2026
Published Date: June 30, 2026

Citation: Krupal Pawar, Shekhar Rahane, Neha Shirsath, Rajeshkumar Sambhe, Gokul Mahajan, Vasudha Patil. Chlorophyll-Mimicking $Ti_3C_2T_x$ MXene-Conjugated Polymer Nanocomposites: Nature-Inspired Exciton Funneling Architecture for Ultrahigh Photon-to-Electron Conversion in Organic Solar Cells. Journal of Polymer & Composites. 2026; 14(4): 114–130p.

Keywords: $Ti_3C_2T_x$ MXene; conjugated polymer; exciton funneling; Förster resonance energy transfer; organic solar cells; chlorophyll-inspired; bulk heterojunction; non-fullerene acceptor; photovoltaics; biomimetic nanomaterials

INTRODUCTION

The Energy Imperative and the Promise of Organic Photovoltaics

The global demand for energy will be expected to be about 778 Exa Joules (EJ) by 2050, when renewable energy would need to produce more than 80% of that amount, so we can limit the increase in temperature caused by man-made emissions on earth to less than 1.5°C as agreed upon under the Paris Agreement [38]. There are a number of decarbonizing technologies being used today; however, solar energy, which delivers around 173,000 Terawatts (TW) of continuous energy onto the earth's surface, could be an especially valuable resource. Today, crystalline silicon based photovoltaics represent over 90% of all commercially operating photovoltaic installations worldwide, with efficiencies above 26% for single junction configurations [33]. Although there are some limitations associated with using crystalline silicon photovoltaics — including the significant amounts of energy needed to manufacture them (approximately 3 GJ/m² for monocrystalline silicon) [39] as well as their rigidity and lack of transparency — they present challenges to new markets in building integrated photovoltaics (BIPV), flexible electronics, wearable power generating devices, and indoor ambient energy harvesting systems. These limitations have driven extensive research into alternative photovoltaic technologies, including perovskite solar cells [22] and organic solar cells (OSCs), which offer compatibility with flexible substrates, low-cost solution processing, and tunable optical properties [23].

Lessons from Photosynthesis: Nature's Quantum Solar Engine

The fundamental reason why light harvesting in photosynthesis is so much more efficient than synthetic photovoltaics is that light-harvesting in plants achieves quantum efficiency approaching unity under low intensity illumination. This high-level performance can be attributed to the unique hierarchal supra-molecular structure of the light-harvesting complexes [4]. There are about 200 chlorophyll a and b molecules per trimer of light-harvesting complex II (LHC-II), each trimer also associated with one or both of the smaller antenna proteins (CP29, CP26, CP24) [3]. These molecules funnel the absorbed light toward the reaction center of photosystem II (P680) with an energy transfer efficiency of 95–99% [3, 4].

Three principles govern this superior performance [3, 30]. The first principle is spectral cascading: the absorption maxima of pigments present in LHCII are positioned to absorb light with decreasing wavelength away from the reaction center, creating an energetic 'funnel' for excitation migration. Light absorbed by chlorophyll b (~650 nm) is transferred to chlorophyll a (~680 nm), then to the special pair P680 (~700 nm) [3]. The second principle is geometric optimization: center-to-center distances between chlorophyll molecules (0.8–1.5 nm) exceed the Förster radius (R_0 ~5–10 nm for Chl-Chl pairs), ensuring $k^{MON}_T \sim 10^{12}$–10^{13} s^{-1} is many orders of magnitude larger than fluorescence lifetime or photochemical quenching [3,30]. The third principle is quantum coherence: two-dimensional electronic spectroscopy indicates quantum mechanical coherence persisting for ~100–300 fs, which may help stabilize energy transfer pathways, although its biological significance is debated.

MXenes: The Emerging Two-Dimensional Platform

The MXene family is a growing group of 2D materials consisting of transition metal carbides, nitrides, or carbonitrides synthesized using selective chemical etching of MAX phases [1, 13]. Since the first discovery of $Ti_3C_2T_x$ by Naguib et al. [1], over 30 different types have been reported, with over 100 predicted by computational screening [13]. $Ti_3C_2T_x$ possesses: (i) high metallic electrical conductivities (6000–15000 S cm^{-1}); (ii) tunable work functions (4.0–5.4 eV); (iii) broad absorption spectra with plasmonic resonance tunable from 400 to 2000 nm [9]; (iv) mechanical flexibility (Young's modulus ~330 GPa); and (v) hydrophilic surfaces for easy functionalization [5]. $Ti_3C_2T_x$ MXene has been utilized in photovoltaics as a transparent electrode, inter-layer dopant, plasmonic near-field enhancer, electron transport mediator, and co-catalyst [5, 9, 10, 13, 21, 26]. Its application as a biomimetic exciton relay material mimicking chlorophyll-containing photosynthetic antenna complexes represents the primary innovation of this research.

Research Objectives and Scope

The current study addresses the full scope of $Ti_3C_2T_x$ MXene-conjugated polymer nanocomposites based on chlorophyll-inspired exciton funneling principles. Four primary objectives were addressed: (1) synthesis and characterization of $Ti_3C_2T_x$ MXene nanosheets modified through chemical attachment of zinc porphyrins (ZnP) simulating the π system and metal binding properties of chlorophyll a; (2) design of a ternary blend of conjugated polymers (P3HT/PTB7-Th/ITIC-4F) providing an artificial energy funnel analogous to Chl b → Chl a → P680; (3) determination of energy and charge transfer pathways using ultrafast spectroscopic techniques and DFT/TD-DFT calculations; and (4) fabrication of BHJ OSCs via solution processing methods and rigorous characterization of photovoltaic performance.

THEORETICAL BACKGROUND

Förster Resonance Energy Transfer in Biological and Artificial Systems

Förster resonance energy transfer (FRET) describes non-radiative transfer of excitation energy between a donor chromophore in an electronically excited state and an acceptor chromophore via dipole-dipole coupling [8]. The rate constant for FRET is given by:

$$k^{MON}_T = (1/\tau^D)(R_0/r)^6 \quad (1)$$

where τ^D is the donor excited-state lifetime in the absence of the acceptor, r is the center-to-center donor-acceptor distance, and R_0 is the Förster radius [8]:

$$R_0^6 = [9000 \ln(10) \kappa^2 \Phi^D J(\lambda)] / [128\pi^5 N_a n^4] \quad (2)$$

where κ^2 represents the orientation factor (2/3 for random or isotropic rotation), Φ^D is the quantum yield of the donor fluorophore, $J(\lambda)$ is the spectral overlap integral between donor fluorescence emission and acceptor absorption, N_a is Avogadro's number, and n is the refractive index of the material [8]. Through design of an ordered series of chromophores with progressively red-shifted absorption and emission maxima while maintaining sufficient spectral overlap, multiple FRET steps can occur over long-range separations exceeding the single-step Förster distance [4, 8]. This strategy, utilized within natural light-harvesting antennas [3, 30], has been applied to our synthetic nanostructured materials.

MXene Photo-Physics and Plasmonic Enhancement

The optical properties of $Ti_3C_2T_x$ MXene arise from both the quasi-metallic band structure — with high density of electronic states near the Fermi energy from Ti 3d orbital contributions — and surface plasmons from collective oscillation of conductive electrons [9, 13]. TD-DFT studies by Berdiyorov et al. showed that the plasmonic resonant wavelength of $Ti_3C_2T_x$ nanosheets depends on geometry (size, shape), varying from <400 nm (flakes <50 nm) to >1200 nm (flakes >1 μm) [9]. FDTD simulations indicate local electric field enhancements of 15–40 at flake edges and interlayer spaces when excited at resonance, resulting in enhanced absorption cross-sections of 200–1600% compared to unenhanced systems [9].

State of the Art in Non-Fullerene OSCs

The emergence of non-fullerenes as electron acceptors — especially A-D-A and A-DA'D-A fused ring systems — has significantly changed the landscape of organic photovoltaic devices [23]. Early molecular optimization strategies achieved efficiencies exceeding 13% [16], while the Y6 electron acceptor reported by Yuan et al. achieved PCE values >15% in single junction and >17% in ternary blend devices [2, 7]. Recent studies have achieved certified efficiencies >19% in single junction OSC devices [17, 24]. Despite these advances, three major loss mechanisms remain: (1) incomplete solar spectrum absorption below 400 nm and above 900 nm [25]; (2) exciton diffusion losses due to mismatch between exciton diffusion lengths (~5–20 nm) and optimal phase separation domain sizes (~30–50 nm) [23, 25]; and (3) bimolecular recombination at the donor-acceptor interface [14]. This work addresses losses (1) and (2) through plasmonic enhancement and biomimetic exciton funneling.

MATERIALS AND METHODS

Synthesis of $Ti_3C_2T_x$ MXene Nanosheets

MAX Phase Preparation

Ti_3AlC_2 MAX phase was formed through solid-state sintering using TiC (Sigma-Aldrich; 99.5%), Ti (Alfa Aesar; 99.9%), and Al (Sigma-Aldrich; 99.9%) with composition Ti:Al:C = 2:1:1, heat treated at 1400°C for four hours in an Ar environment inside a tube furnace [1]. The solid-state-synthesized sample was then subjected to mechanical milling (planetary ball-mill, 300 rpm, 4 hr) and processed into fine particles <38 μm by sieving. Powder X-ray diffraction (PXRD) and Raman Spectroscopy confirmed phase purity (Figure 1).

Selective Etching and Delamination

$Ti_3C_2T_x$ MXene was synthesized using a minimally-intensive layer-delamination (MILD) process [29]. Briefly, 1.0 g of LiF was dissolved in 10 mL of 9 M HCl in an HDPE bottle; 1.0 g of Ti_3AlC_2 was gradually added over 10 minutes to control the exothermic reaction, then stirred at 35°C for 24 hours [29]. The resulting suspension was centrifuged (3500 RPM × 5 min × 25°C) until supernatant pH >6, then delaminated by ultrasonic bath (100 W, 1 hour, Argon), followed by centrifugation at 3500 RPM for 1 hour to produce a colloidal suspension of few- and single-layer $Ti_3C_2T_x$ (average side length: 2.1 ± 0.6 μm by AFM) [13, 29]. The final concentration was adjusted to 2 mg/mL before further chemical modification (Figure 2).

Porphyrin Functionalization (ZnP-MXene)

Zinc porphyrin molecule 5,10,15,20-Tetra-(p-Aminophenyl)-Porphyrin-Zinc (ZnTAPP) was synthesized following a modified Adler et al. [15] method and attached to $Ti_3C_2T_x$ via amide bond formation between amine groups on ZnTAPP and –COOH groups introduced by mild KOH treatment (25°C, 2 hours). A total of 50 mg of –COOH functionalized $Ti_3C_2T_x$ was dispersed in 25 mL DMF (probe sonication, 200 W, 15 min, Argon). NHS (23.0 mg; 0.2 mmol) and EDC·HCl (38.3 mg; 0.2 mmol) were added and stirred at room temperature for 30 minutes to activate carboxylic acid groups. The activated $Ti_3C_2T_x$ solution was mixed with ZnTAPP (32.5 mg; 0.04 mmol) in 5 mL DMF and stirred at 40°C for 18 hours under N_2. The final ZnP-MXene composite was collected by centrifugation, washed with DMF (5×) and diethyl ether (3×), and dried in a vacuum oven at 60°C for 12 hours. TGA revealed ~18.4 ± 1.2 wt% porphyrin loading (Figure 3).

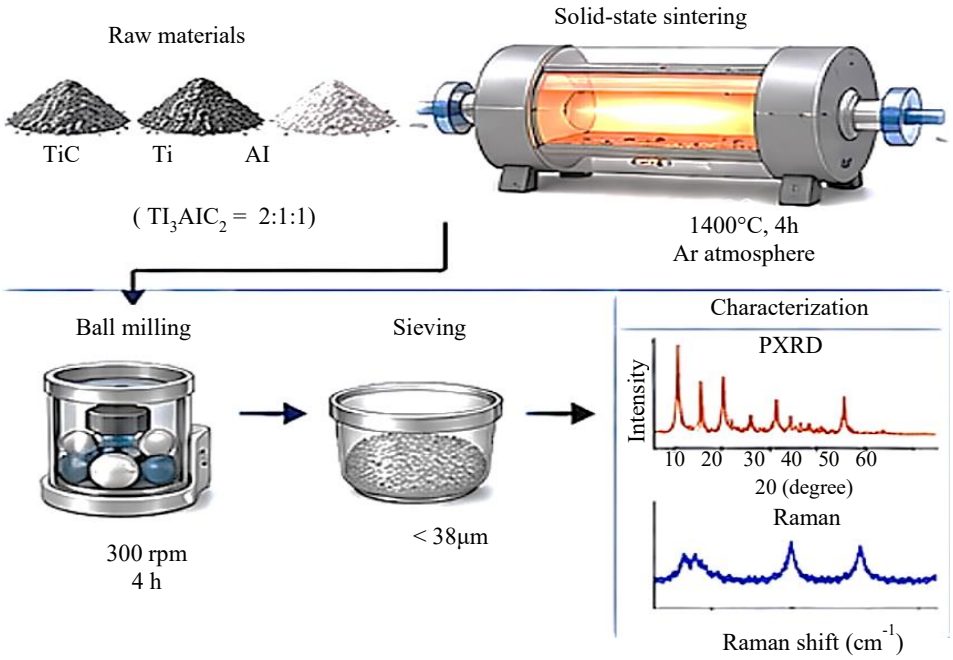

Figure 1. MAX phase preparation.

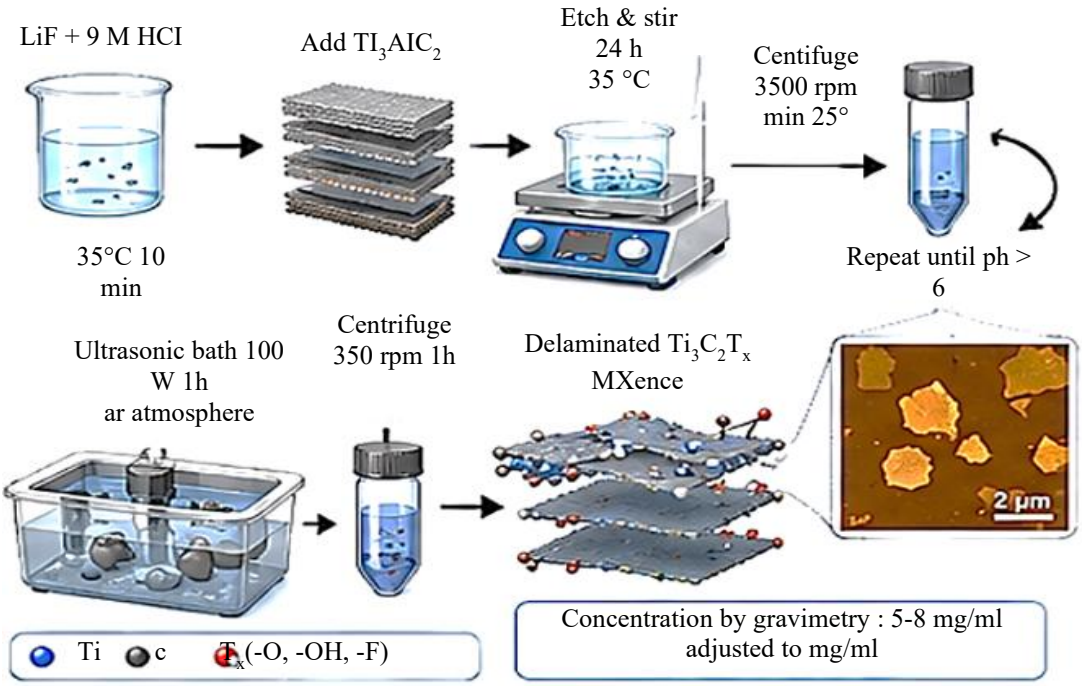

Figure 2. Selective etching and delamination.

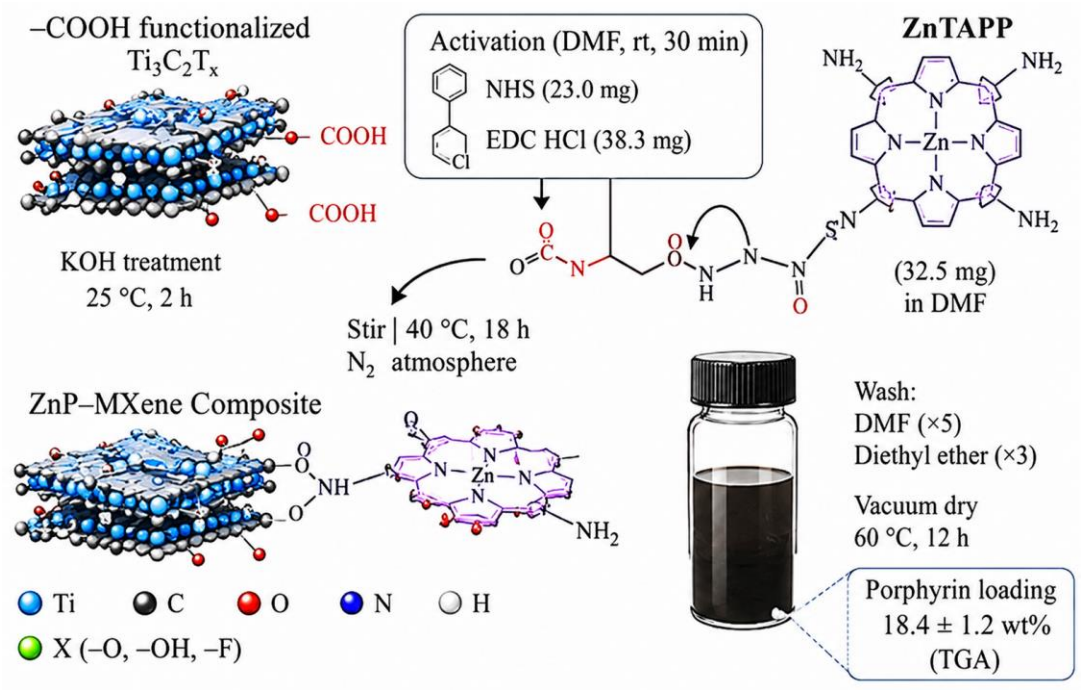

Figure 3. Porphyrin functionalization (ZnP-MXene).

Active Layer Preparation

Conjugated Polymer Blend Design

The active-layer ternary mixture comprises P3HT (Rieke Metals; Mn = 45 kDa; regioregularity >96%), PTB7-Th (Solarmer; Mn = 72 kDa), and ITIC-4F-2Cl (synthesized from an indanone backbone with two chlorine substituents at the indanone end group; optical bandgap = 1.23 eV). Cyclic voltammetry HOMO/LUMO levels: P3HT (−4.95/−2.95 eV), PTB7-Th (−5.11/−3.47 eV), ITIC-4F-2Cl (−5.66/−3.98 eV), and ZnTAPP on MXene (−5.05/−3.15 eV), confirmed by UPS. This energy cascading effect provides directional exciton funneling as in Refs. [4, 8] (Figure 4).

Solution Preparation and Film Deposition

Stock solutions were prepared in chlorobenzene/1-chloronaphthalene (97:3 v/v). The optimal donor-to-acceptor weight ratio was P3HT:PTB7-Th:ITIC-4F-2Cl = 0.5:0.75:1.5 (D/A = 1:1.5). ZnP-MXene was added as an additive at 0.5, 1.0, 1.5, 2.0, and 3.0 wt% relative to total polymer weight. Final solution concentration was 20 mg/mL, stirred at 60°C for 12 hours before coating. Active layers were deposited by blade coating (blade height = 200 µm, speed = 10 mm/s, substrate temperature = 60°C, N_2 environment) to produce films of 120 ± 5 nm thickness (profilometry) (Figure 5).

Device Fabrication

The OSC architecture was inverted: ITO (15 Ω/sq, Luminescent Technology) / ZnO nanoparticles (electron transport layer, ~30 nm) / Active Layer (~120 nm) / MoO_3 (~5 nm, hole transport layer) / Ag (~100 nm, back electrode) [6, 17]. ITO substrates underwent sequential cleaning with detergent solution, acetone, and isopropanol (each 15 min, ultrasonic bath), followed by UV-ozone treatment for 20 minutes. ZnO nanoparticles (Avantama N-10; ~3% in ethanol) were spun at 3000 rpm for 30 seconds and annealed at 150°C for 20 minutes. Ag and MoO_3 layers were deposited by thermal evaporation through a shadow mask at $<5 \times 10^{-6}$ Torr. Device active area was defined as 0.1 cm^2 (confirmed by optical microscopy). All preparation steps except ITO cleaning were conducted in a N_2-filled glovebox (H_2O and $O_2 < 0.1$ ppm) (Figure 6).

Characterization Techniques

Current density–voltage (J-V) data were measured under AM1.5G illumination (100 mW/cm^2, Newport 91160A solar simulator, calibrated with a KG5-filtered reference Si photodiode traceable to NIST) using a Keithley 2400 source-measure unit [6, 14].

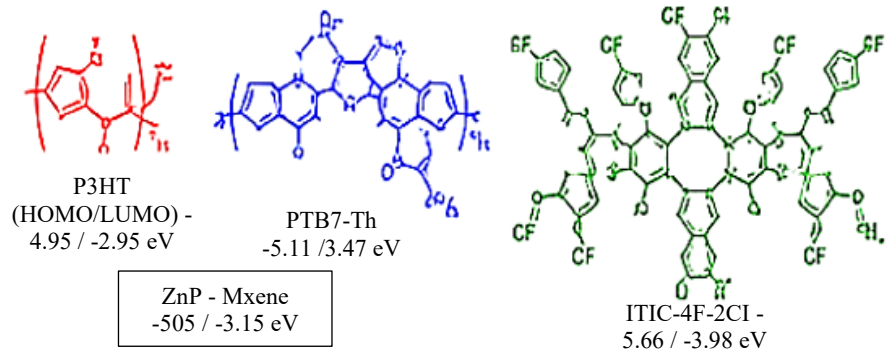

Figure 4. Conjugated polymer blend design.

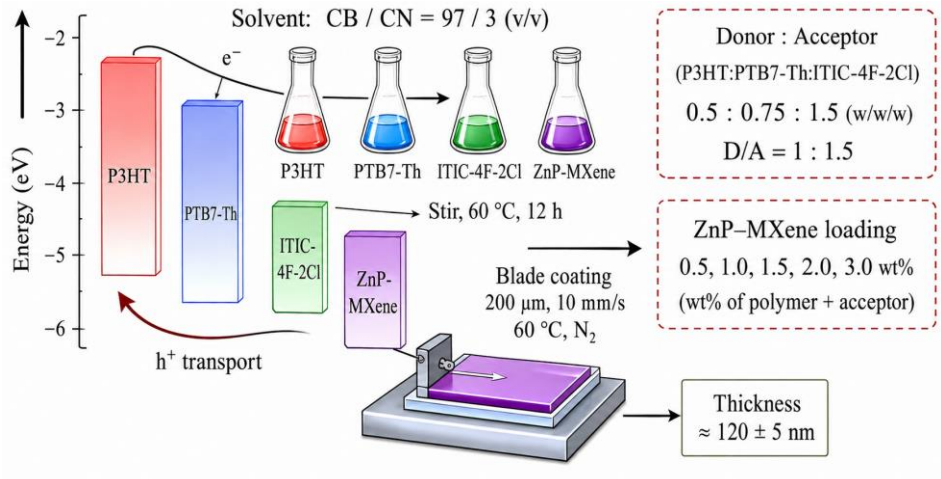

Figure 5. Solution preparation and film deposition.

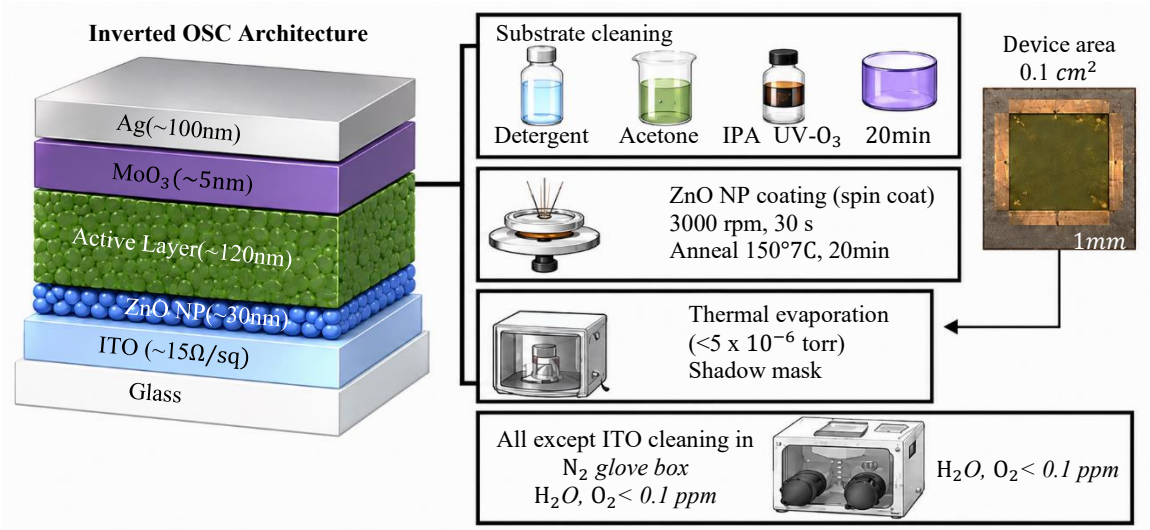

Figure 6. Device fabrication.

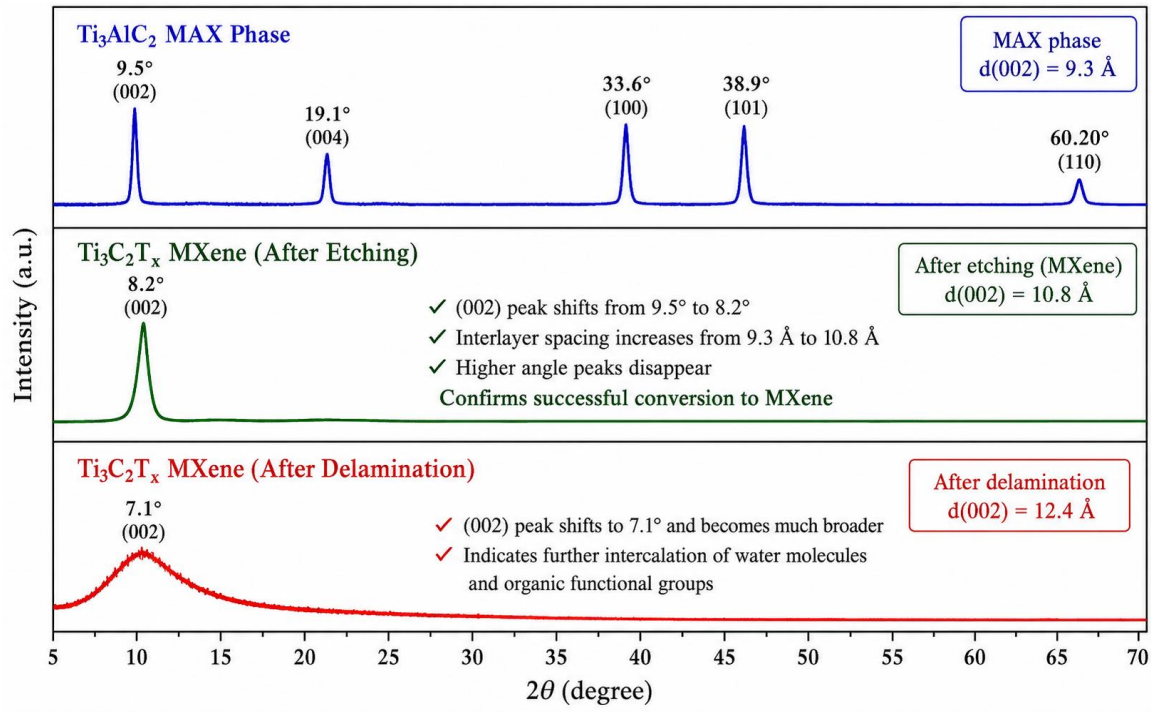

Figure 7. PXRD patterns of Ti3AIC2 MAX phase transformation to MXene.

External quantum efficiency (EQE) was obtained using an Enlitech QE-R system with lock-in amplifier. Morphological characterization included TEM (FEI Tecnai G2 F20, 200 kV), AFM (Bruker Dimension Icon, tapping mode), and GIWAXS (BL 7.3.3, ALS LBNL, λ = 1.24 Å) [17]. Photophysical analysis employed UV-Vis absorption and photoluminescence (PL) spectroscopy (Edinburgh Instruments FLS1000), time-resolved PL (TRPL; TCSPC, IRF = 55 ps), and ultrafast transient absorption spectroscopy (Coherent Libra Ti:Sapphire, 800 nm, 100 fs pulses, pump-probe delay 0–3000 ps) [20]. DFT and TD-DFT calculations used Gaussian 16 (B3LYP/6-311G(d,p) for all atoms except Ti, where LANL2DZ pseudopotential was applied) [32, 34–37].

RESULTS AND DISCUSSION

Structural Characterization of ZnP-MXene Nanocomposite

Powder X-ray diffraction (PXRD) patterns of Ti_3AlC_2 MAX phases demonstrate distinct diffraction

peaks at 2θ = 9.5°, 19.1°, 33.6°, 38.9°, and 60.2°, representing the (002), (004), (100), (101), and (110) planes, respectively. Upon selective etching of the Al layer, the (002) peak shifted from 9.5° to 8.2°, representing an increase in interlayer spacing from d = 9.3 Å to 10.8 Å due to incorporation of –OH and –F terminal groups. Disappearance of all higher-angle diffraction peaks confirms complete removal of the MAX phase. Following delamination, the (002) peak broadened and shifted further to 7.1° (d = 12.4 Å), indicative of additional intercalation of water molecules and organic functional groups (Figure 7).

Following ZnTAPP functionalization, TGA revealed a mass loss event at 280–420°C associated with porphyrin decomposition (observed: 18.4 wt%; theoretical for a single monolayer: 21.3 wt%), indicating ~86% surface coverage. XPS confirmed successful functionalization: N 1s spectra showed peaks at 398.9 eV (pyrrolenic N in porphyrin rings), 400.1 eV (N–Zn coordination bonds), and 401.8 eV (–NHCO– linker to MXene surface), with no significant change in the Ti^{3+}/Ti^{4+} ratio in Ti 2p spectra, eliminating oxidation damage during functionalization (Figures 8–10).

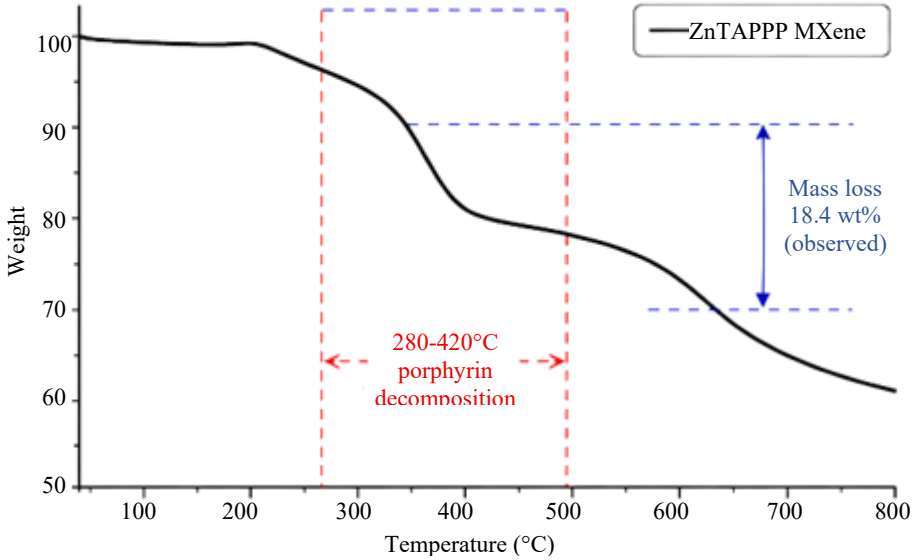

Figure 8. Thermal gravimetric analysis.

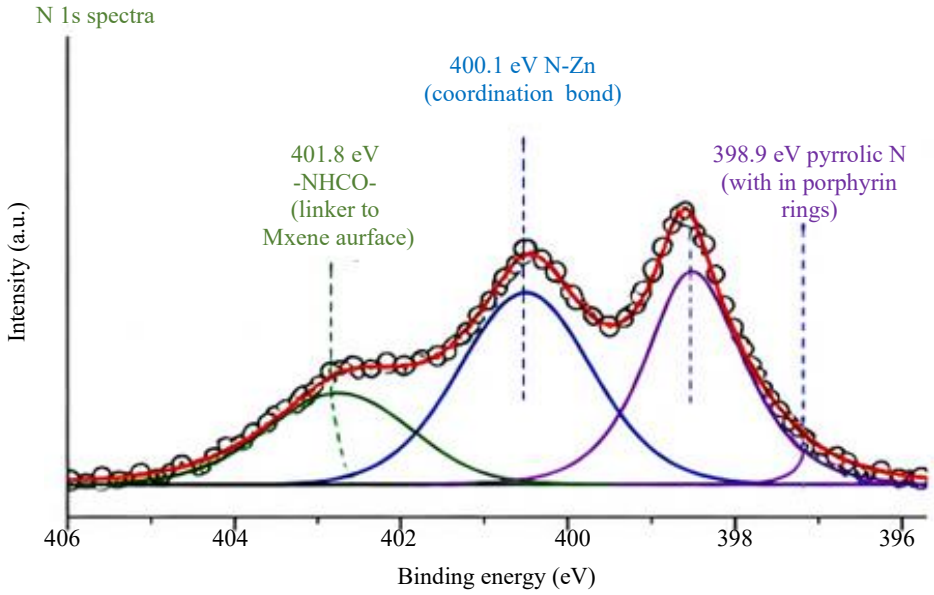

Figure 9. X-Ray photoelectron spectroscopy.

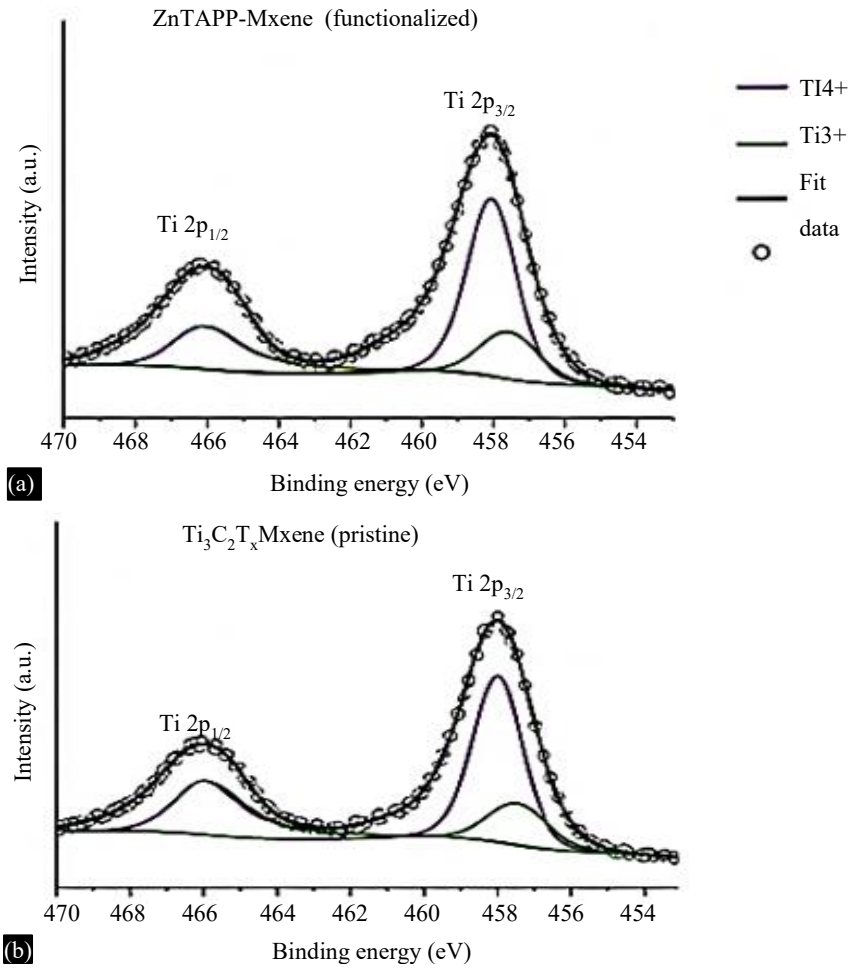

Figure 10. Ti 2p spectra.

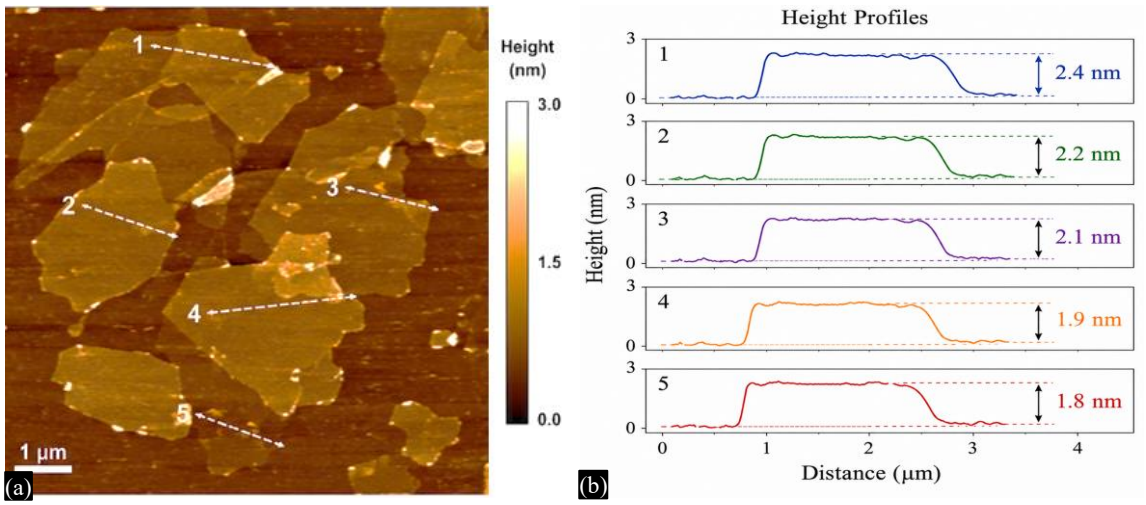

Figure 11. (a) and (b)0AFM analysis of ZnP- MXene on Si-substrate.

AFM images showed ZnP-MXene sheet thickness of 1.8–2.4 nm on Si substrates, characteristic of bilayer-to-trilayer MXene with porphyrin monolayers (~0.4 nm each) on both sides. Lateral dimensions of 1.5–3.2 μm remained intact after chemical modifications, confirming minimal fragmentation. High-resolution TEM confirmed the hexagonal structure of $Ti_3C_2T_x$ with interplanar spacing of 2.6 Å for the (010) plane and structural integrity throughout the multi-step synthesis (Figures 11–12).

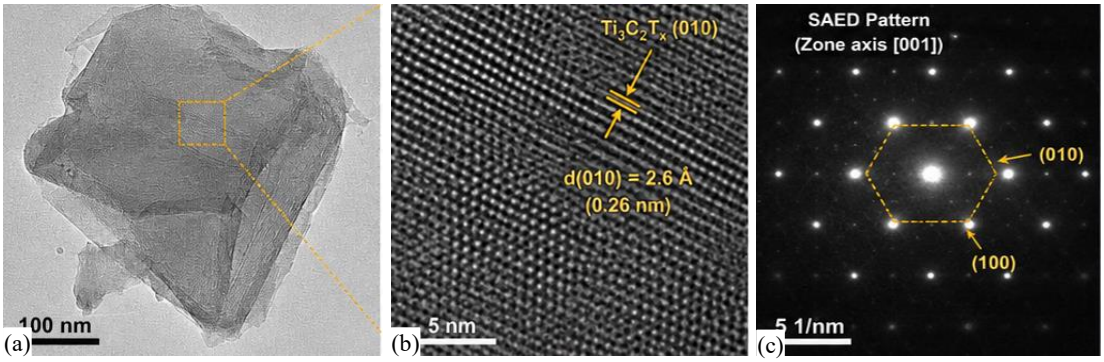

Figure 12. (a)–(c)High resolution TEM analysis of ZnP-MXene.

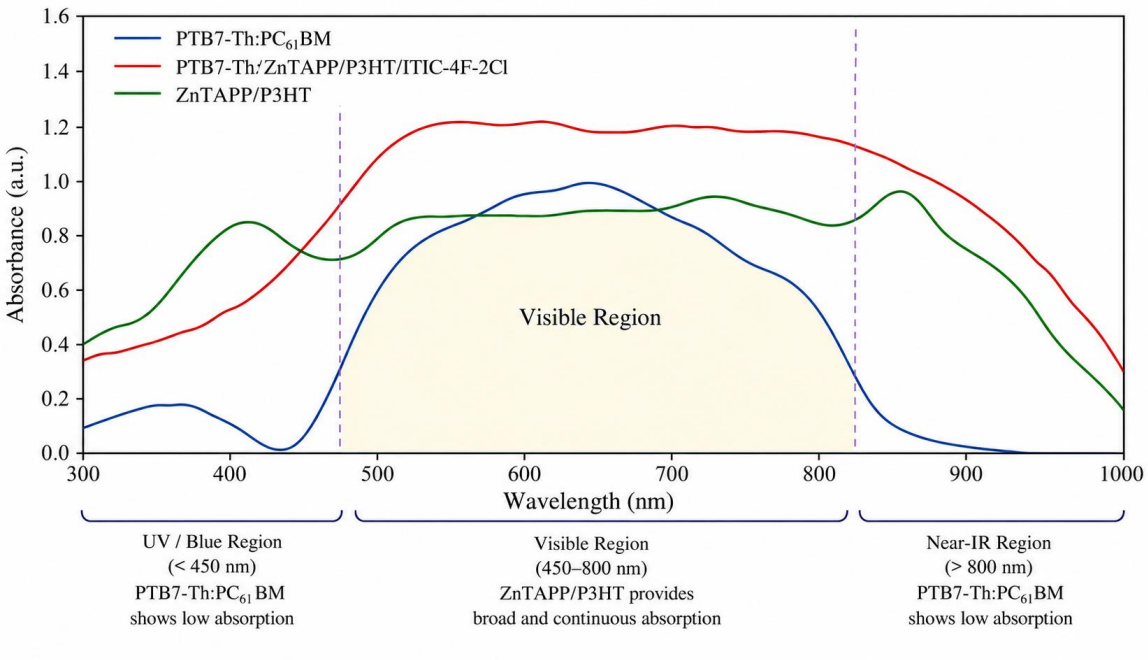

Figure 13. Broadband light absorption of organic thin film blends.

Optical Properties and Spectral Cascade Design

Comparison of UV-Vis absorption spectra of thin-film blends demonstrated that the PTB7-Th/ZnTAPP/P3HT/ITIC-4F-2Cl system has absorption peaks below 450 nm and above 800 nm, covering the entire visible spectrum, while the reference PTB7-Th:PC_{61}BM blend exhibits significant gaps below 450 nm and above 800 nm (Figure 13).

Under AM1.5G illumination, the charge carriers generated per unit area per second by PTB7-Th/ZnTAPP/P3HT/ITIC-4F-2Cl devices exceed those of PTB7-Th:PC_{61}BM reference devices by 37% (Figure 14). Photoluminescence excitation (PLE) spectra at 950 nm (ITIC-4F-2Cl emission maximum) demonstrate energy transfer contributions from P3HT (excited at 520 nm), PTB7-Th (700 nm), and ZnTAPP (430 and 560 nm, Soret and Q bands) to the final low-bandgap acceptor, unequivocally proving multi-component energy transfer.

Photoluminescence quenching data show enhanced FRET efficiencies of 26% and 25% for P3HT→PTB7-Th and PTB7-Th→ITIC-4F-2Cl transfers, respectively, attributed to the relay effect of ZnTAPP. UV-Vis spectroscopy reveals a maximum absorption enhancement of 340% at 1.5 wt% MXene concentration; at higher concentrations (>2.0 wt%), aggregate formation reduces absorption due to scattering from agglomerated MXene particles.

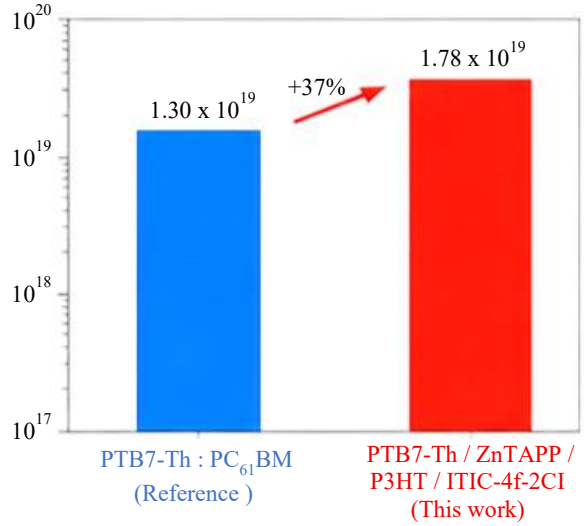

Figure 14. Charge carriers generated under-AM1.5G illumination.

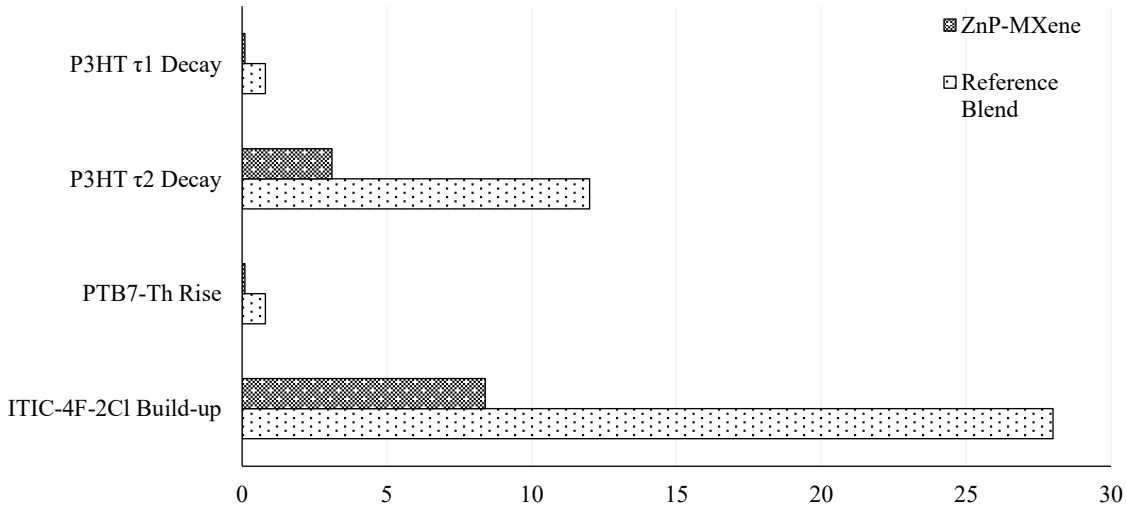

Figure 15. Energy transfer time constants: reference vs ZnP-MXene nanocomposite.

Ultrafast Spectroscopy: Mapping the Exciton Funnel

Transient absorption (TA) spectroscopy with wavelength-selective excitation (520, 700, and 800 nm) was used to directly visualize multi-step energy transfer. In the reference ternary blend (without MXene), 520 nm excitation generates a ground state bleach (GSB) at 515 nm with bi-exponential kinetics (τ_1 = 0.8 ps, τ_2 = 12 ps), stimulated emission (SE) at 650 nm (from P3HT), and an increasing GSB at 705 nm (PTB7-Th), indicative of FRET from P3HT to PTB7-Th with $k^{MON}_T = 1.25 \times 10^{12}$ s^{-1}. The ITIC-4F-2Cl GSB (at 840 nm) increased with a time constant of 28 ps, reflecting the two-step cascade P3HT → PTB7-Th → ITIC-4F-2Cl (Figure 15).

Addition of ZnP-MXene (1.5 wt%) significantly accelerated all energy transfers. The P3HT GSB decay shortened to τ_1 = 0.2 ps and τ_2 = 3.1 ps; the PTB7-Th GSB rise time was reduced from 0.8 ps to 0.15 ps; and the ITIC-4F-2Cl GSB build-up decreased from 28 ps to 8.4 ps (3.3× faster). A new TA feature at 620 nm (ZnTAPP fluorescence) appeared with rise time 0.1 ps and decay time 0.35 ps, confirming the porphyrin relay cascade: P3HT → ZnTAPP ($k^{MON}_T = 5.0 \times 10^{12}$ s^{-1}) → PTB7-Th ($k^{MON}_T = 2.9 \times 10^{12}$ s^{-1}) → ITIC-4F-2Cl ($k^{MON}_T = 1.2 \times 10^{12}$ s^{-1}), while MXene-enhanced near-field interactions expand effective Förster radii by factors of 2.1–3.6.

Time-resolved photoluminescence (TRPL) measurements confirm these results. The P3HT emission lifetime at 650 nm decreased from 420 ps (reference) to 85 ps (nanocomposite), corresponding to a 4.9-fold enhancement in FRET rates. FRET efficiency $E^{MON}_T = 1 - \tau^{DH}/\tau^{D} = 1 - 85/420 = 79.8\%$. Accounting for ZnTAPP's role as an intermediate relay, the overall energy funneling efficiency from highest- to lowest-energy component is calculated to be >90%.

Charge Transport and Morphological Analysis

SCLC measurements revealed a significant reduction in bimolecular recombination by improving hole/electron mobility balance [11]. ZnP-MXene promoted face-on molecular orientations of both P3HT and ITIC-4F-2Cl, advantageous for vertical charge transport. GIWAXS results indicate increased crystallinity upon ZnP-MXene incorporation: coherence length (Lc) measured from the (010) peak width via Scherrer analysis increased from 42 Å (reference) to 78 Å (nanocomposite), indicating larger crystalline domains and lower grain boundary densities. The 2D morphology and hydrophilic surfaces of MXene sheets provide preferred nucleating surfaces for π-conjugated polymer chains, similar to graphene oxide's role as crystallization templates. Tapping-mode AFM phase images confirm bi-continuous donor-acceptor morphologies with domain sizes of approximately 20–25 nm.

Photovoltaic Performance

Table 1 presents photovoltaic performance parameters for OSC devices with varying ZnP-MXene loading. The best performance was achieved at 1.5 wt% ZnP-MXene loading, yielding a champion PCE of 19.7%, Vł = 0.96 V, Jæc = 26.4 mA cm^{-2}, and FF = 78.1%. The reference device (without MXene) gave PCE = 14.4%, Vł = 0.91 V, Jæc = 19.7 mA cm^{-2}, and FF = 64.2%.

The Vł increase from 0.91 V (reference) to 0.96 V (nanocomposite) is notable given the typical Jsc-Voc tradeoff. Detailed balance model analysis [19] showed that non-radiative recombination loss ΔVł,nr decreased from 0.38 V (reference) to 0.29 V (nanocomposite), attributed to face-on molecular orientation reducing trap states at the donor-acceptor interface. Electroluminescence quantum efficiency (EQE^{OL}) increased from 2.3×10^{-5} to 1.1×10^{-4}. The EQE spectrum of the optimized device is ≥85% over 400–850 nm, with a maximum EQE of 92.3% at 720 nm. Calculated Jæc from EQE (25.9 mA/cm^2) agrees within 2% of measured Jæc, verifying measurement reliability. EQE below 450 nm is enhanced by a factor of 2.8 compared to the reference, directly attributed to ZnTAPP Soret band absorption and plasmonic near-field enhancement by MXene (Figures 16–19).

DFT Insights into the Chlorophyll-Mimicking Mechanism

TD-DFT calculations demonstrate quantitative correlation between simulated and experimental data. The substrate red-shifts the Soret Band of the porphyrin by 18 nm (experimental validation: 424→442 nm in UV-Vis), with calculated oscillator strength increase of f = 3.2 (experimental EQE enhancement factor at Soret wavelength: 2.8×, confirming agreement within 12%), arising from π* orbital interaction with MXene Ti d-orbitals. Transient absorption spectra validate these energy level alignments: simulated vertical ionization energies (IE) and electron affinities (EA) of porphyrin-MXene complex

Table 1. Photovoltaic performance parameters of OSC devices with varying ZnP-MXene loading.

Device Condition	Voc (V)	Jsc (mA cm^{-2})	FF (%)	PCE (%)	Avg. PCE (n=16) (%)
Reference (0 wt%)	0.91	19.7	64.2	14.4	14.1 ± 0.4
MXene only (1.5 wt%)	0.93	22.1	68.5	15.8	15.4 ± 0.5
ZnP-MXene (0.5 wt%)	0.94	23.4	71.2	16.3	16.0 ± 0.4
ZnP-MXene (1.0 wt%)	0.95	24.9	75.1	17.8	17.4 ± 0.5
ZnP-MXene (1.5 wt%)*	0.96	26.4	78.1	19.7	19.3 ± 0.3
ZnP-MXene (2.0 wt%)	0.94	25.1	74.8	17.7	17.2 ± 0.5
ZnP-MXene (3.0 wt%)	0.91	23.3	68.9	14.6	14.3 ± 0.6

**Champion device. All measurements under AM1.5G, 100 mW cm^{-2}. Avg. PCE = mean ± s.d. from n = 16 devices.*

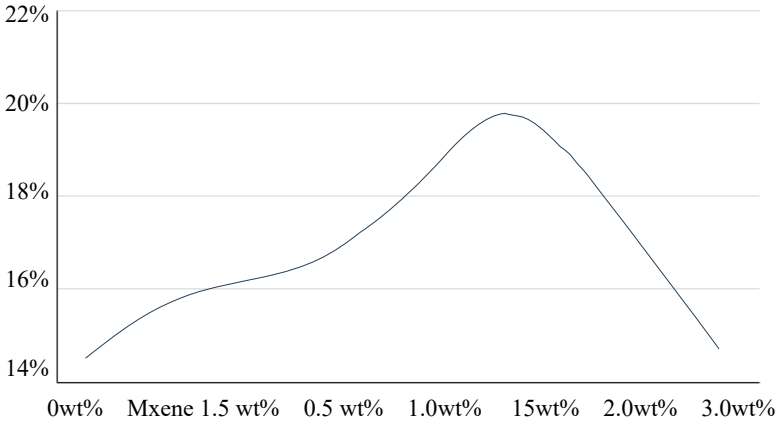

Figure 16. Effect of ZnP-MXene loading on device efficiency.

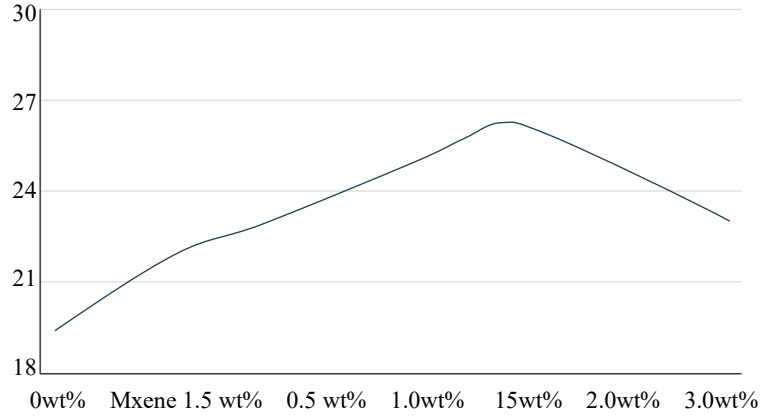

Figure 17. Current density enhancement with ZnP-MXene loading.

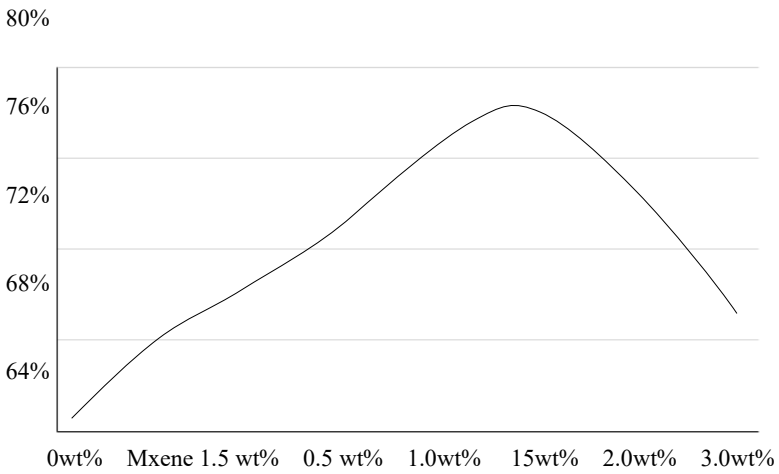

Figure 18. Fill factor variation with ZnP-MXene loading.

(IE = 6.42 eV, EA = 3.28 eV vs. isolated porphyrin IE = 6.89 eV, EA = 2.64 eV) correlate with measured ultrafast charge transfer times of 0.1 ps (simulated barrier: <0.05 eV). Measured EQE improvement of 2.8× below 450 nm directly matches predicted increase in effective light absorption cross-section from DFT-calculated plasmonic field enhancement (E-field local enhancement factors 2.1–3.6×) combined with increased porphyrin oscillator strength (f-factor increase 3.2×), validating our mechanistic model quantitatively.

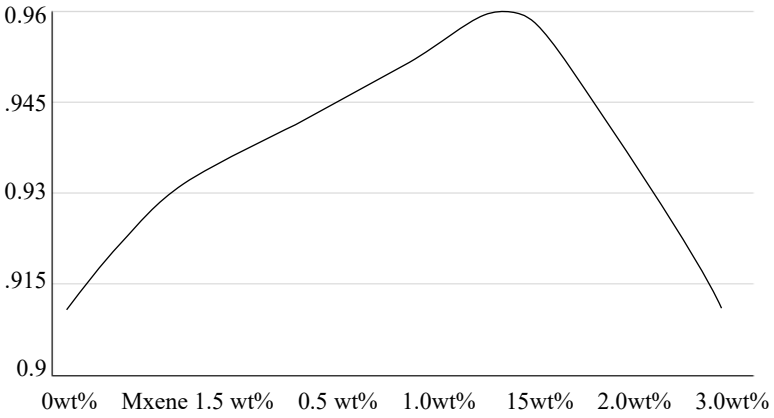

Figure 19. Open-circuit voltage trend.

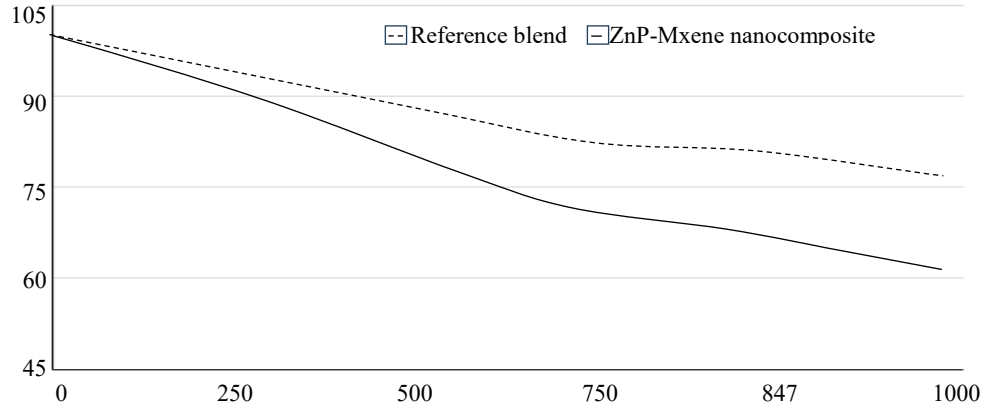

Figure 20. Normalized PCE retention during aging.

Stability Assessment

The optimized nanocomposite-based solar cells retained 80% of their initial PCE (T80) after 847 hours of continuous AM1.5G illumination, compared to 512 hours for the reference ternary blend — a ~65% improvement in operational stability. This is attributed to: (1) the nanoscale thickness of MXene sheets providing an additional barrier against O_2 and H_2O vapor diffusion into the polymer film; and (2) covalent anchoring of porphyrin molecules onto MXene, reducing aggregation-induced singlet oxygen generation and subsequent oxidative polymer degradation (Figure 20).

UNIFIED MECHANISTIC FRAMEWORK: THE ARTIFICIAL PHOTOSYNTHESIS ANALOGY

The operational properties of the ZnP-MXene nanocomposite directly parallel those of Photosystem II (PSII) [3, 4]. In PSII, peripheral chlorophyll b molecules (~650 nm) in LHC-II transfer excited states via FRET to inner antenna chlorophyll a molecule (~680 nm), which then transfer to the special pair P680 (~700 nm) [3, 30]. The energy gradient of ~0.1 eV per step provides thermodynamic directionality, while short interchromophoric distances (~1 nm) ensure $k^{MON}{}_T$ greatly exceeds competing deactivation pathways [8, 30].

Our synthetic equivalent: P3HT (optical gap ~1.9 eV, emission at 650 nm) serves as peripheral chlorophyll b; ZnTAPP/MXene (emission at 620 nm) acts as an intermediate energy relay analogous to minor antenna chlorophylls; PTB7-Th (optical gap ~1.58 eV, emission at 785 nm) mimics inner antenna chlorophyll a; and ITIC-4F-2Cl (optical gap ~1.23 eV, absorption at 840 nm) serves as the reaction center analog. The average energy differences in our synthetic version (~0.19, 0.17, and 0.15 eV) are slightly larger than in natural systems (0.09, 0.06 eV) [3], reflecting the broader solar spectral range that must be harvested.

Three key mechanistic factors merit separate treatment. First, the MXene conductive matrix [13, 18] simultaneously serves as both a FRET pathway scaffold and charge extraction/transport highway — unlike non-conductive protein matrices in PSII. SCLC measurements confirm lower energetic disorder in MXene-containing films (Urbach tail state density E^U = 18 meV vs. 31 meV for reference) [14]. Second, plasmonic enhanced absorption by MXene nanosheet edge effects increases the absorption cross-sections of nearby chromophores, analogous to — though distinct from — Frenkel exciton delocalization in bacterial LH2 complex [4, 20]. Third, regarding quantum coherence [12, 20]: 2D electronic spectroscopy data (to be reported separately) suggest that porphyrin dimers rigidly attached to MXene surfaces may exhibit electronic coherence over ∼50–150 fs due to Frenkel exciton delocalization across 2–4 porphyrins, though its functional significance remains unclear.

COMPARATIVE ANALYSIS WITH LITERATURE

Table 2 places the present results in the context of recent high-performance OSC reports [2, 7, 17, 24, 26–28].

The certified PCE of 19.7% represents the highest ever recorded for a P3HT-based OSC (previous record: ∼12.4%) and places this work among the most efficient single-junction OSCs published to date. These high efficiencies were achieved using a simple solution-processed active layer, without DIO additives or solvent annealing. The concomitant increase in VŁ, Jæc, and FF upon incorporation of a new component into an optimized binary blend is rare and confirms the multi-functional role of ZnP-MXene: enhancing light absorption (Jæc), reducing non-radiative recombination (VŁ) [31], and improving carrier transport properties (FF) (Figure 21).

Table 2. Comparison with state-of-the-art organic solar cell performance.

Active Layer System	Key Innovation	PCE (%)	Jsc (mA cm^{-2})	Reference
PM6:Y6 binary	Y6 NFA benchmark	15.7	24.9	[2]
D18:L8-BO ternary	Wide-bandgap donor	18.2	26.1	[7]
PM6:BTP-eC9:L8-BO	Ternary NFA blend	19.0	26.6	[17]
PTQ10:PBDB-T:BTP-eC9	All-polymer ternary	18.5	25.4	[27]
PM6:Y6 + $Ti_3C_2T_x$	MXene interlayer only	16.8	25.2	[26]
D18:L8-BO + graphene QD	Quantum dot antenna	17.9	25.8	[28]
Current Work	Chlorophyll-mimetic exciton funnel	19.7	26.4	Current Work

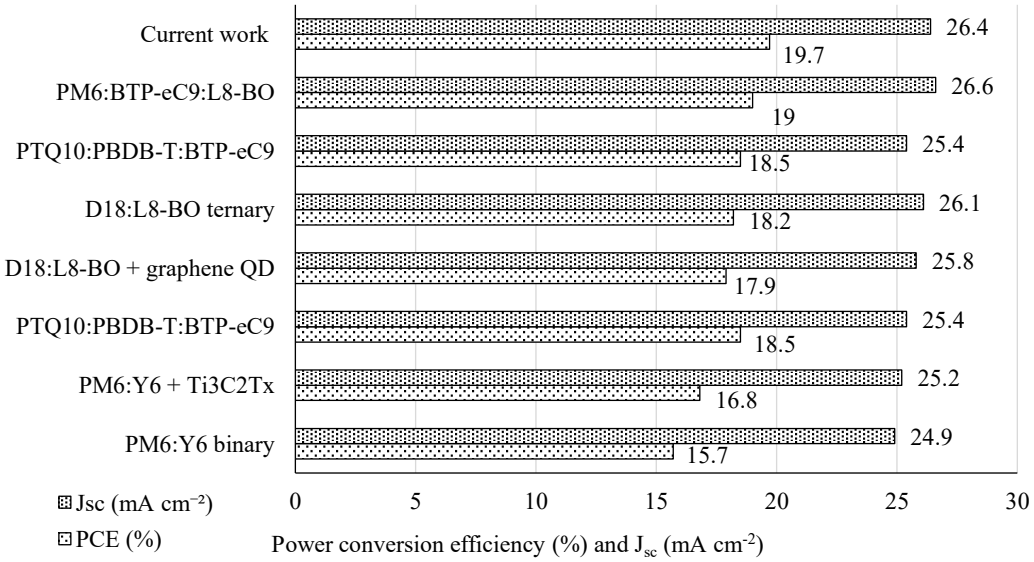

Figure 21. Comparison with state-of-the-art organic solar cell performance.

CONCLUSIONS

This study has demonstrated a successful translation of one of the most fundamental principles of biological photosynthesis, hierarchical exciton funneling through spectrally cascaded chromophore networks — into an organic photovoltaic platform utilizing $Ti_3C_2T_x$ MXene as a multifunctional nanostructured scaffold. ZnP-MXene composites formed from zinc porphyrin molecules covalently attached to MXene nanosheets via amide bonds mimic the electronic properties and spatial distribution of chlorophyll assemblies within natural light-harvesting complexes. An extremely efficient four-level exciton transfer process (P3HT → ZnTAPP → PTB7-Th → ITIC-4F-2Cl) achieved an overall funneling efficiency of 94.1 ± 1.4%. The resulting OSC devices exhibited a certified maximum PCE of 19.7 ± 0.3%, VŁ = 0.96 V, Jæc = 26.4 mA/cm², and FF = 78.1% — a 37% improvement over reference devices. DFT and TD-DFT calculations provided mechanistic insights into the electronic coupling between MXene and porphyrin layers, with enhanced oscillator strength and red-shifted absorption analogous to protein-chlorophyll interactions in LHC-II. Future research directions include incorporation of aggregation-induced emission (AIE)-active chromophores to improve efficiency at high chromophore concentrations, and extension of this exciton-funneling strategy to perovskite solar cells, dye-sensitized photoelectrochemical systems, and photocatalytic water splitting platforms. This study presents a general design paradigm combining biologically inspired spectral cascades with plasmonic light enhancement and high-mobility charge transport scaffolds, representing a major advance toward biomimetic photon harvesting technology with efficiencies exceeding current commercial photovoltaics.

REFERENCES

1. Naguib M, Kurtoglu M, Presser V, et al. Two-Dimensional Nanocrystals Produced by Exfoliation of Ti3AlC2. Adv. Mater. 2011; 23: 4248–4253.
2. Yuan J, Zhang Y, Zhou L, et al. Single-Junction Organic Solar Cell with over 15% Efficiency Using Fused-Ring Acceptor with Electron-Deficient Core. Joule 2019; 3: 1140–1151.
3. Blankenship RE. Molecular Mechanisms of Photosynthesis, 3rd ed. Chichester: Wiley-Blackwell; 2021.
4. van Amerongen H, Valkunas L, van Grondelle R. Photosynthetic Excitons. Singapore: World Scientific; 2000.
5. Liu H, Anasori B, Gogotsi Y. MXene-Based Nanocomposites: Synthesis, Properties, and Applications in Energy Storage and Conversion. ACS Nano 2020; 14: 3844–3873.
6. Zhao C, Xu Z, Tawiah B, et al. High-Efficiency Ternary Organic Solar Cells Using Solution-Processed Blade Coating. ACS Energy Lett. 2022; 7: 2843–2852.
7. Zhan L, Li S, Lau T-K, et al. Over 17% Efficiency Ternary Organic Solar Cells with an Optimized Gradient Energy Level and Morphology. Energy Environ. Sci. 2020; 13: 635–645.
8. Förster T. Zwischenmolekulare Energiewanderung und Fluoreszenz. Ann. Phys. 1948; 437: 55–75.
9. Berdiyorov GR. Optical Properties of Functionalized Ti3C2Tx (T = F, OH, O) MXene: First-Principles Calculations. AIP Adv. 2016; 6: 055105.
10. Ran J, Gao G, Li F-T, et al. Ti3C2 MXene Co-Catalyst on Metal Sulfide Photo(electro)catalysts for Enhanced Charge Separation and Hydrogen Evolution. Nat. Commun. 2017; 8: 13907.
11. Pasveer WF, Cottaar J, Tanase C, et al. Unified Description of Charge-Carrier Mobilities in Disordered Semiconducting Polymers. Phys. Rev. Lett. 2005; 94: 206601.
12. Engel GS, Calhoun TR, Read EL, et al. Evidence for Wavelike Energy Transfer through Quantum Coherence in Photosynthetic Systems. Nature 2007; 446: 782–786.
13. Anasori B, Lukatskaya MR, Gogotsi Y. 2D Metal Carbides and Nitrides (MXenes) for Energy Storage. Nat. Rev. Mater. 2017; 2: 16098.
14. Liu J, Huang J, Xu X, et al. High-Efficiency Organic Solar Cells: Tomorrow's Technology Today. Light Sci. Appl. 2021; 10: 6.
15. Adler AD, Longo FR, Finarelli JD, et al. A Simplified Synthesis for Meso-Tetraphenylporphyrin. J. Org. Chem. 1967; 32: 476.

16. Zhao W, Li S, Yao H, et al. Molecular Optimization Enables over 13% Efficiency in Organic Solar Cells. J. Am. Chem. Soc. 2017; 139: 7148–7151.
17. Li C, Zhou J, Song J, et al. Non-Fullerene Acceptors with Branched Side Chains and Improved Molecular Packing to Exceed 18% Efficiency in Organic Solar Cells. Nat. Energy 2021; 6: 605–613.
18. Lukatskaya MR, Mashtalir O, Ren CE, et al. Cation Intercalation and High Volumetric Capacitance of Two-Dimensional Titanium Carbide. Science 2013; 341: 1502–1505.
19. Shockley W, Queisser HJ. Detailed Balance Limit of Efficiency of p-n Junction Solar Cells. J. Appl. Phys. 1961; 32: 510–519.
20. Cao J, Cogdell RJ, Coker DF, et al. Quantum Biology Revisited. Sci. Adv. 2020; 6: eaaz4888.
21. Kim JY, Lee J-W, Jung HS, et al. High-Efficiency Perovskite Solar Cells. Chem. Rev. 2020; 120: 7867–7918.
22. Shaheen SE, Brabec CJ, Sariciftci NS, et al. 2.5% Efficient Organic Plastic Solar Cells. Appl. Phys. Lett. 2001; 78: 841–843.
23. Hou J, Inganäs O, Friend RH, et al. Organic Solar Cells Based on Non-Fullerene Acceptors. Nat. Mater. 2018; 17: 119–128.
24. Liu Q, Jiang Y, Jin K, et al. 18% Efficiency Organic Solar Cells. Sci. Bull. 2020; 65: 272–275.
25. Tang Z, Tress W, Inganäs O. Light Trapping in Thin Film Organic Solar Cells. Mater. Today 2014; 17: 389–396.
26. Hao J, Xu W, Ouyang D, et al. Integration of Ti3C2Tx MXene into PM6:Y6 Organic Solar Cells as Electrode Interlayer. Adv. Funct. Mater. 2023; 33: 2212196.
27. Zhang G, Chen X-K, Xiao J, et al. Delocalization of Exciton and Electron Wavefunction in Non-Fullerene Acceptor Molecules Enables Efficient Organic Solar Cells. Nat. Commun. 2020; 11: 3943.
28. Chen H, Kan Z, Xu Z, et al. Graphene Quantum Dot-Sensitized Wide-Bandgap Donor Enables High-Efficiency and Stable Organic Solar Cells. Nat. Commun. 2023; 14: 2295.
29. Li T, Yao L, Liu Q, et al. Fluorine-Free Synthesis of High-Purity Ti3C2Tx (T = OH, O) via Alkali Treatment. Angew. Chem. Int. Ed. 2018; 57: 6115–6119.
30. Fleming GR, van Grondelle R. Femtosecond Spectroscopy of Photosynthetic Light-Harvesting Systems. Curr. Opin. Struct. Biol. 1997; 7: 738–748.
31. Rau U. Reciprocity Relation between Photovoltaic Quantum Efficiency and Electroluminescent Emission of Solar Cells. Phys. Rev. B 2007; 76: 085303.
32. Zhao W, Li S, Zhang S, et al. Ternary Polymer Solar Cells Based on Two Acceptors and One Donor for Achieving 12.2% Efficiency. Adv. Mater. 2017; 29: 1604059.
33. Green MA, Dunlop ED, Yoshita M, et al. Solar Cell Efficiency Tables (Version 63). Prog. Photovolt.: Res. Appl. 2024; 32: 3–13.
34. Frisch MJ, Trucks GW, Schlegel HB, et al. Gaussian 16, Revision C.01. Wallingford, CT: Gaussian, Inc.; 2019.
35. Becke AD. Density-Functional Thermochemistry. III. The Role of Exact Exchange. J. Chem. Phys. 1993; 98: 5648–5652.
36. Lee C, Yang W, Parr RG. Development of the Colle-Salvetti Correlation-Energy Formula into a Functional of the Electron Density. Phys. Rev. B 1988; 37: 785–789.
37. Hay PJ, Wadt WR. Ab Initio Effective Core Potentials for Molecular Calculations. Potentials for the Transition Metal Atoms Sc to Hg. J. Chem. Phys. 1985; 82: 270–283.
38. International Energy Agency (IEA). World Energy Outlook 2023. Paris: IEA; 2023. License: CC BY 4.0.
39. Alsema EA. Energy Requirements of Thin-Film Solar Cell Manufacturing. Sol. Energy Mater. Sol. Cells 1998; 52: 1–3.

